Supplementary materials: elemental diversity in high entropy alloy MoNbTaVW: complex He diffusion paths and improved radiation resistance

Zhehao Chen[1], Guanying Wei[1], Kenichiro Mizohata[1], Eryang Lu[1*], Jesper J A Byggmästar[1], Guo Wei[1], Xudong An[1,2], Loïc Perrière[3], Jean-Philippe Couzinié[3], Zhi-Wei Huang[4], Che-Wei Tsai[4,5], Jien-Wei Yeh[4,5], Kai H Nordlund[1], Flyura Djurabekova[1,6] and Filip Tuomisto[1,6]

1: Department of Physics, University of Helsinki, P.O. Box 43, FI-00014, Helsinki, Finland

2: College of Mechanical Engineering, University of South China, Hengyang, 421001, China

3: Université Paris Est, Institut de Chimie et des Matériaux Paris-Est (UMR7182), CNRS, UPEC, 2-8 rue Henri Dunant, F-94320, Thiais, France

4: Department of Materials Science and Engineering, National Tsing Hua University, Hsinchu 30013, Taiwan

5: High Entropy Materials Center, National Tsing Hua University, Hsinchu 30013, Taiwan

6: Helsinki Institute of Physics, University of Helsinki, Gustaf Hällströmin katu 2, 00014 Helsinki, Finland

**Corresponding author: eryang.lu@helsinki.fi*

1. Surface morphologies

The X-ray diffraction (XRD) spectrum and electron backscatter diffraction (EBSD) mapping showed a single body-centered cubic (BCC) phase structure with an average grain size of ~100 μm. Surface scanning electron microscopy coupled with energy-dispersive X-ray spectroscopy (SEM-EDS) elemental mapping images are displayed in Fig. **S1**. The refractory high-entropy alloy (RHEA) MoNbTaVW displays micro-segregations of Mo, Nb, and V at grain boundaries, which is already reported before in the reference[1]. The ternary MoNbTa medium-entropy alloy (RMEA) exhibit small compositional gradients. Table **S1** shows the nominal total chemical concentration of the three materials given by the EDS mapping. All elements show near equimolar both in RHEA and RMEA.

Table **S1**. EDS analysis of average elemental concentrations (at. %) in three materials

Elements/materials	RHEA	RMEA	Ta
Mo	20.1	33.5	/
Nb	20.0	33.1	/
Ta	19.0	33.4	100
W	21.0	/	/
V	19.9	/	/

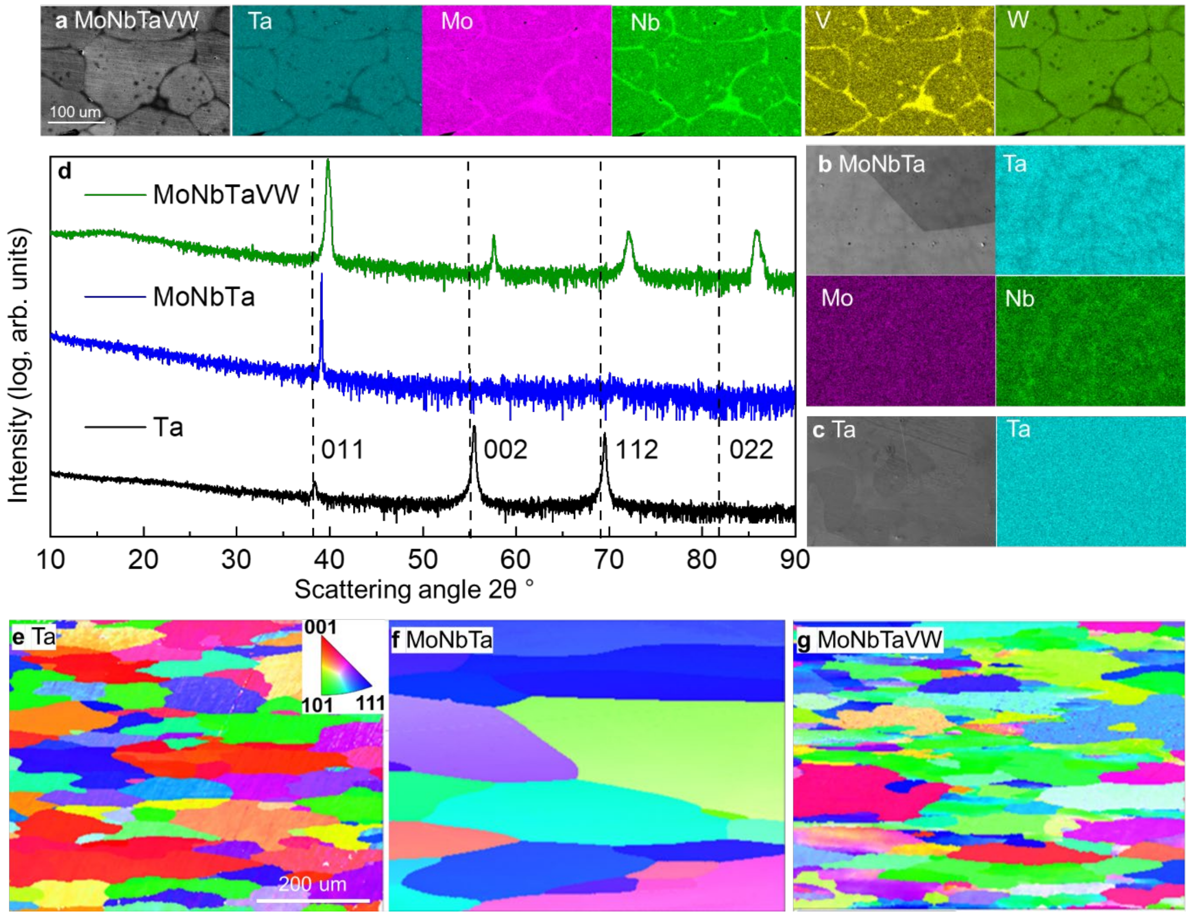

Fig.**S1** Surface morphologies and crystal structures characterized by SEM and EDS mapping (**a - c**) of three materials, all sharing the same scale bar, XRD (**d**), where the vertical dashed lines mark the angular positions of reflections for bulk unstrained Ta

(ICDD file 96-151-2545), grain size and orientation mapping by EBSD (**e - g**), sharing the same scale bar).

2. ERDA calibration

Elastic recoil detection analysis (ERDA) with filter foil were done with 30 MeV $^{35}Cl^{+6}$ beam. Energy was chosen to maximize probing depth and depth resolution of He in the samples. The detector was at 50° angle relative to ion beam direction. Sample was tilted 50°, with 30° incident and 20° exit angle relative to sample surface. Havar foil to filter heavy recoils and scattered beam was 4.0 μm thick. Detector with rectangular collimator (2 x 7 mm^2) was at 10 cm from sample to reduce kinematic energy spread. With this setup, He can be analyzed up to ~300 nm. Data was acquired in list mode to monitor desorption of the H and He and changes of the depth profiles of He. All ERDA raw data are showed in Fig.**S2**.

For energy and concentration calibration, Si sample (Fig.**S3**) implanted with 30 keV He and with 2 x 10^{16} at/cm^2 fluence was used. Energy calibration was based on surface H and He peak energies from this sample. Depth and energy of He peak was estimated with SRIM-2013.

Depth profiles of He(helium) in samples were calculated using SRIM stopping forces for Havar and samples. Yield at different depths were converted to concentrations with unscreened ERDA cross sections, but energy straggling and possible multiple scattering effect were not taking account in the depth profiles and depth profiles should be regarded as indicative only. Conversion of the energy spectrum to depth profile was done using python script with stopping tables generated with SRIM-2013.

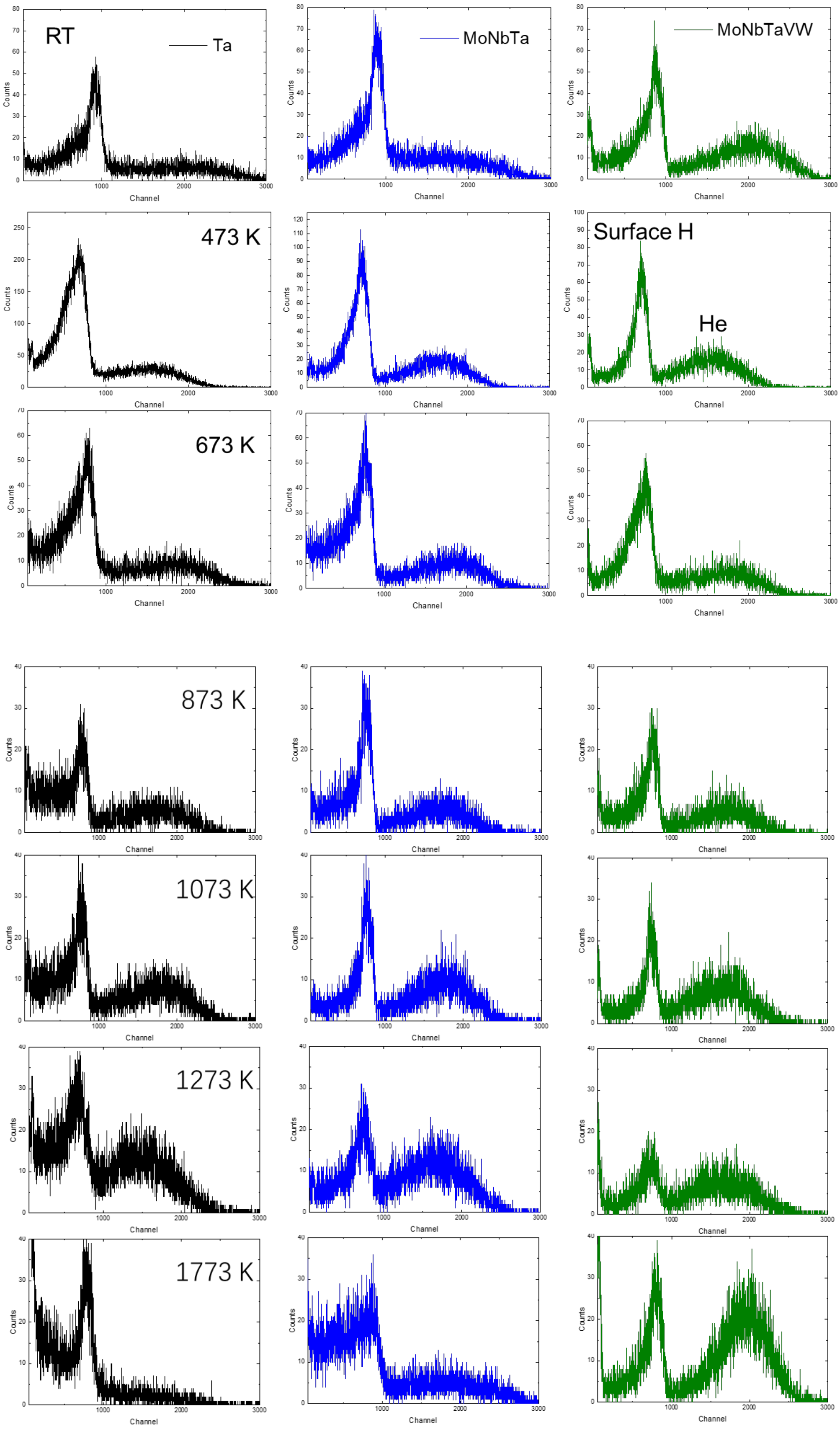

Fig.**S2**. ERDA raw data of three materials from RT-1773 K. The spectrum shows peaks from He and surface Hydrogen (H).

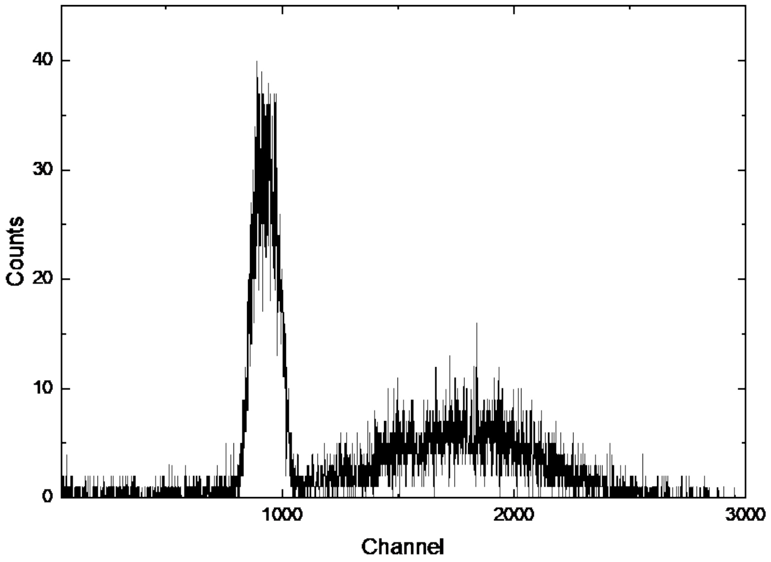

Fig.**S3**. ERDA raw data of an example of Si reference

3. Study of channeling effects on penetration depth.

As noted in the main text, both the He depth distribution after RT irradiation (Fig. 1 **a**) and the vacancy-trapped He damage profile (Fig. 1 **b-f**) seem to be shifted and broaden relative to the prediction by SRIM (Fig. **S4**). This could because of the originate from a combined influence of sample surface angular small misalignment and ion channeling [2]. During annealing from 473 K to 1273 K, He is trapped by vacancies. However, the He peak in all three samples shifts tens of nanometer in the same direction after each annealing step. This is most likely a measurement uncertainty due to a slight misalignment of the sample surface. Since all samples are placed in the same holder after each annealing step, and ERDA depth profiles are highly sensitive to the incident angle, such a peak shift can occur.

Channeling[2] has also shown to effect for ion penetration depths (range profiles) in polycrystalline solids considerably when compared to amorphous materials [3, 4]. Since metals are always polycrystalline, this means that channeling effects are very likely to affect the ion range profiles in them. Here we performed simulations to analyze the channeling effect.

3.1. Simulation method

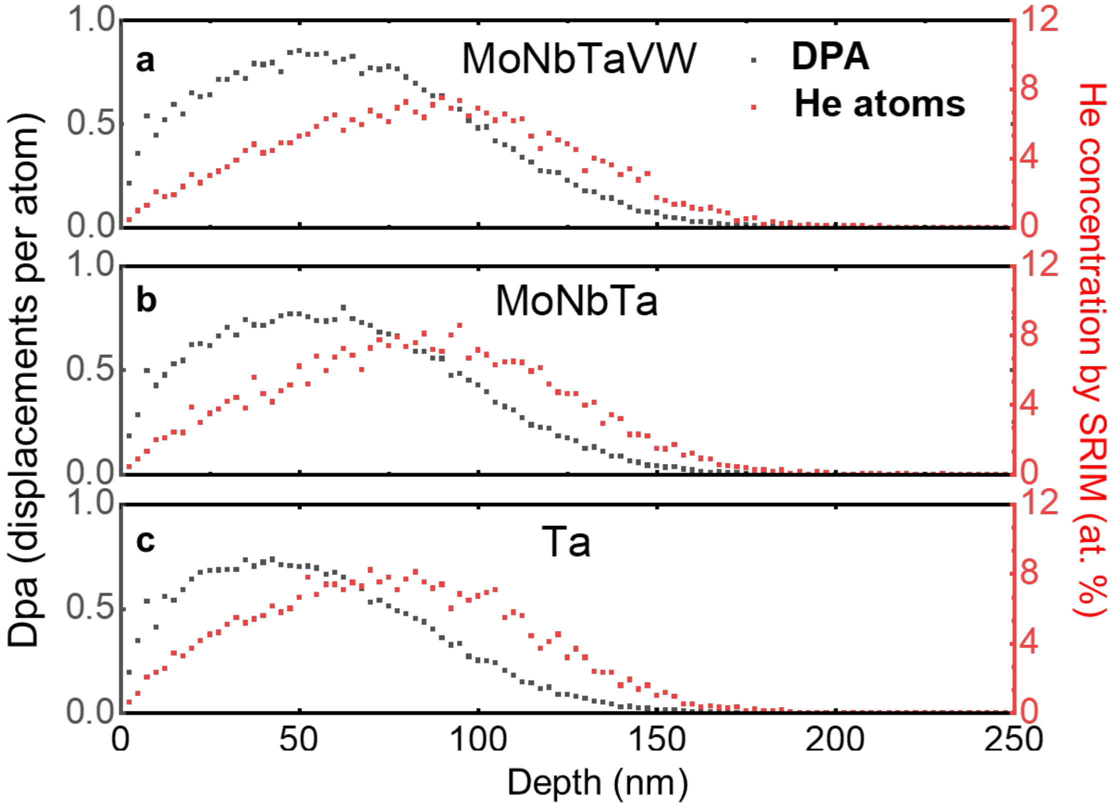

Fig.**S4**. SRIM simulation of 25 keV He concentration and irradiation damage (DPA) depth distribution in three materials

To assess the effect of channeling for 25 keV He ions impinging on polycrystalline Ta, MoNbTa or MoNbTaVW, we simulated ion penetration depths with the MDRANGE code [5], similar to the approach described in detail in Ref. [3]. In brief, the ions were impinging on 001 surface-oriented cells with the BCC crystal structure. To determine penetration depths in other crystal directions, the incoming ion direction was tilted and the range was calculated as the projected range. For comparison with SRIM (which doesn't have any crystal structure), some simulations were carried out into a cubic 3 nm amorphous cell, created by placing atoms in random positions to obtain the correct density, except ensuring no atom was closer than 2.1 Å from each other. The alloy materials were created by randomizing the atom type, however, ensuring that the final number of atoms was as close to equiatomic as possible (since the number of atoms is discrete, the exact number of atoms of each type could vary by 1 in some cells). The crystalline cells in the alloy systems had 432 atoms, which was by testing found sufficiently large to describe the variation in random atom positions with respect to ion ranges.

All simulations used electronic stopping powers obtained from the SRIM2013 code for the corresponding material. Most simulations used the recently published quantum mechanics-based NLH interatomic potentials[6]; to compare with SRIM some of the amorphous material runs were also calculated with the older ZBL potential [7] used by SRIM. The random thermal displacements were generated using a Debye temperature of 225 K as described in the Appendix of Ref.[8]. The lattice constants used were as obtained from the experimental XRD measurements Ta: 3.31 Å, MoNbTa: 3.25 Å, MoNbTaVW: 3.20 Å.

To determine ranges in a fully randomly oriented polycrystal, some calculations were carried out by selecting the initial directions in the 100-110-111 triangle in reciprocal space, that covers all crystallographically nonequivalent directions in a cubic systems. The choice of directions was done by sampling the θ angle off 001 evenly by solid angle sin(θ) dθ. However, as shown by the EBSD maps in the Fig.**S1**, it is not certain whether the grains in the actual polycrystals have evenly distributed surface orientation.

Hence we also simulated ranges in the 100, 111, 110, 102 and 112 crystal directions that appear frequently in the EBSD maps.

3.2. Results: effect of channeling

Results for range profiles in Ta are shown in Fig. **S5** and for the MoNbTaVW RHEA in Fig. **S6**. Results for the MoNbTa are very similar to these two cases, and hence are not shown.

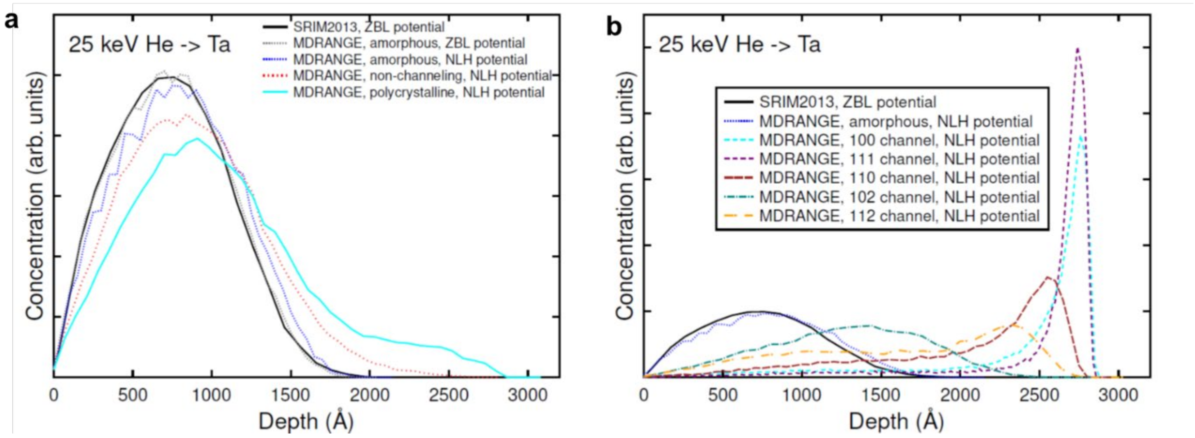

Fig. **S5**. Range profiles for 25 keV He ions in Ta simulated with the SRIM and MDRANGE codes. **a** amorphous and non-channeling directions, **b** results including some low-index crystal directions. The curves are area-normalized.

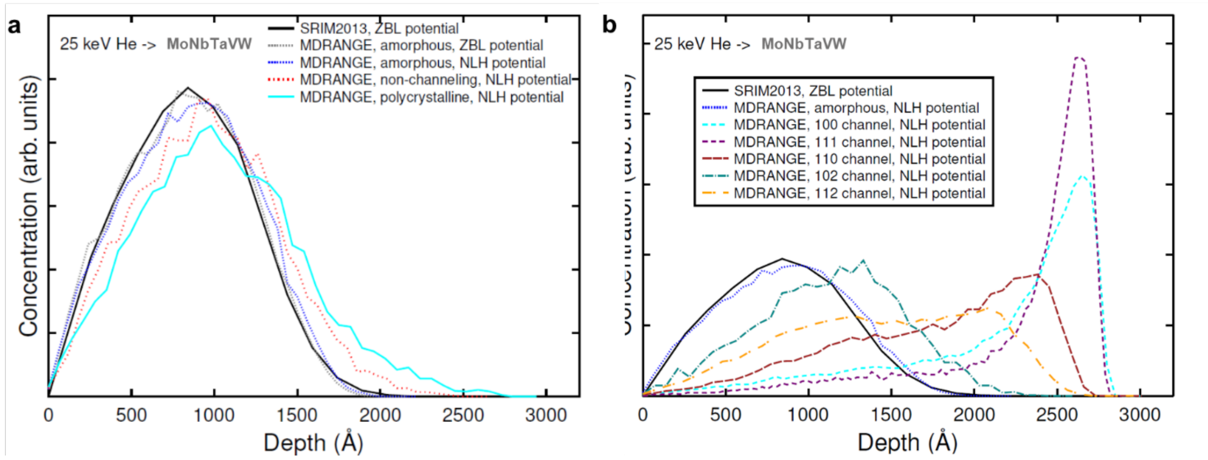

Fig. **S6**. Range profiles for 25 keV He ions in MoNbTaVW high-entropy alloy simulated with the SRIM and MDRANGE codes. **a** amorphous and non-channeling directions, **b** results including some low-index crystal directions. The curves are area-normalized.

The results show that, as expected, the SRIM and MDRANGE results for amorphous material simulated with the ZBL potential agree very well with each other. Using the newer NLH potential leads to slightly longer ranges. The ion ranges in low-index channeling directions are much longer than those for amorphous material, as expected from channeling theory [2]. In the RHEA, the channeling peaks are clearly wider than for Ta, which is because the variation in atom mass and number leads to stronger scattering than for Ta only.

Most interesting, however, is that the range distribution for polycrystalline material is clearly different from the amorphous one. This is because the channels are wide, and hence the probability to end up in a channel is high even for randomly oriented polycrystals. This is illustrated by the channeling maps for in Fig. **S7**, which shows strong channeling in especially the 100, 110 and 111 directions, and that there is significant planar channeling between the low-index directions.

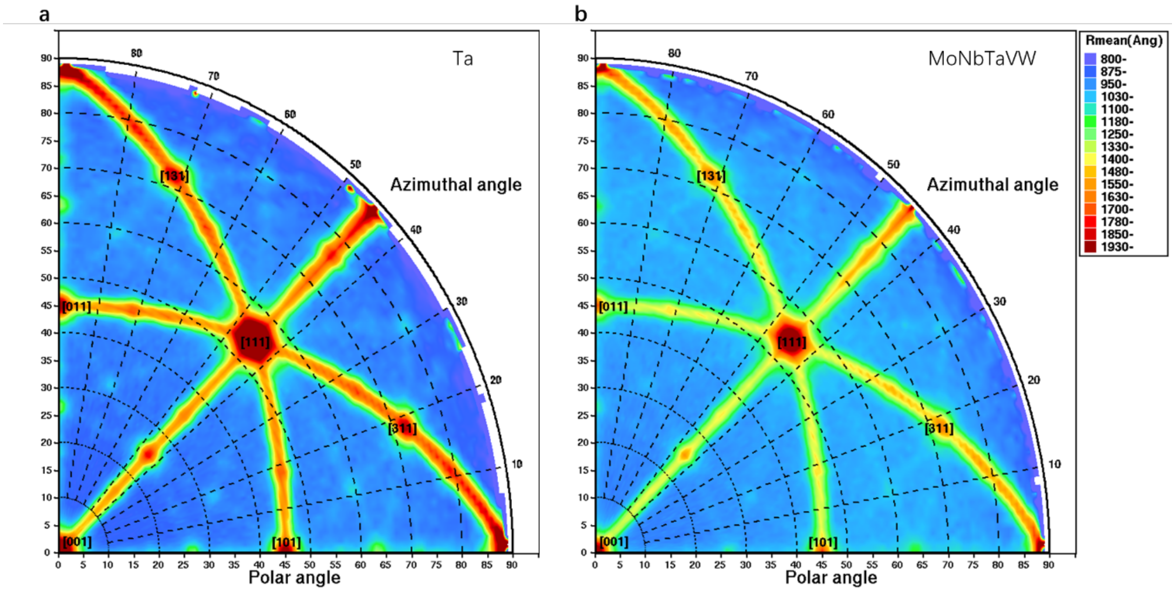

Fig. **S7** Channeling map for 25 keV He ions on Ta (a) and RHEA MoNbTaVW (b). The values for the highest polar angles close to 90 degrees are strongly affected by surface scattering effects and are not meaningful in the current context.

3.3. Results: comparison with experiments.

We also compare the range profiles directly with experiments. The results in Fig. **S8** show that the experimental range distribution differ clearly from the SRIM and amorphous materials result. The polycrystalline profile is closer to the experiments. However, all the simulated profiles for the experimental fluence of 5x10^{16} ions/cm^2 are clearly above the experimental one, indicating that He diffusion at room temperature.

The experimental EBSD maps show that a marked fraction of the crystal grains seems to have a low-index crystal orientation. This may indicate that the surface normal directions are not evenly distributed, but have a predominance of low-index directions. If this is the case, the range profile would have a stronger contribution from these directions than the random “polycrystalline” sample. To test this hypothesis, we made a weighted sum of the range profiles of the polycrystalline, 100, 111, 110, 102 and 112 range distributions. The sum was constructed as

$$C_{\text{weighted}}(z) = 0.4C_{\text{poly}}(z) + 0.05C_{100}(z) + 0.05C_{111}(z) + 0.2C_{110}(z) + 0.3C_{102}(z) + C_{112}(z)$$

When still assuming 40% loss of He, one obtains a good agreement with the experimental range profile, Fig. **S8**. We emphasize that these coefficients were not obtained by a systematic optimization procedure, and considering that the 100 and 111 range profiles are quite similar, many other combinations of coefficients would likely offer an equally good or even better agreement with experiments. This comparison just serves to illustrate the point that if low-index surface normal crystal directions are prevalent in a polycrystalline sample, the range profiles may be strongly affected by this towards longer ranges.

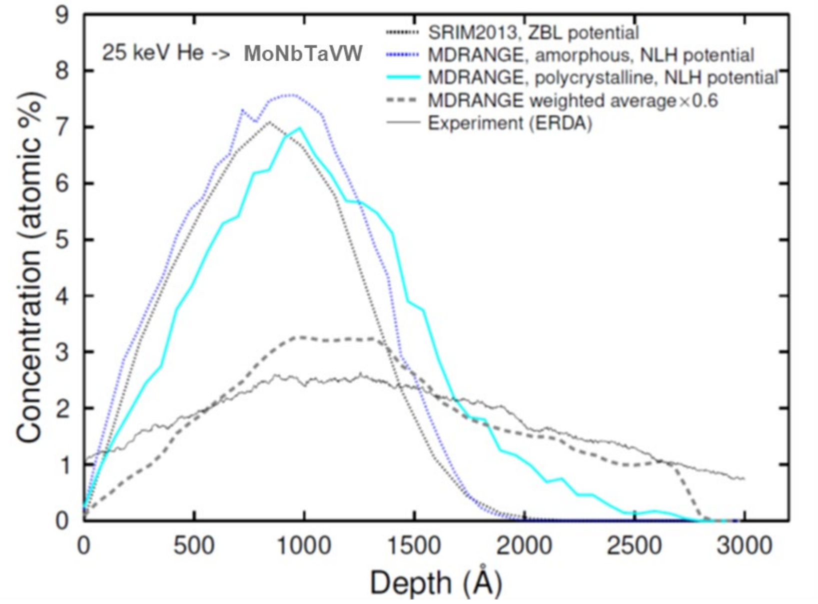

Fig. **S8**. Comparison of simulated and experimental range profiles for the RHEA.

4. Diffusion parameters extracted from MD simulation

Several diffusion parameters can be extracted from the MD simulation as described in the main text. The average mean squared displacement (MSD), $\boldsymbol{r^2(t)}$, defined by $\boldsymbol{r^2(t)} = \frac{1}{N}\sum_{i=1}^{N}[r_i(t) - r_i(0)]^2$ is plotted in Fig. **S9 a**, where t the diffusion time and $\boldsymbol{r_i}(t)$ is the position of the i-th He atom at time t, N is the total He atoms 27. The average trajectory length $L(t)$, reflects the average total path length traveled by the particles, regardless of direction, is computed by summing the stepwise displacements of each atom at every simulation timestep. For each atom i, $L_i(t) = \sum_{j=1}^{M}\left|r_i(t_j) - r_i(t_{j-1})\right|$, where M is the number of frames up to time t, and $\boldsymbol{r_i}(t_j)$ is the position of atom i at frame j. The average trajectory length is then obtained by averaging over all N atoms: $L(t)=\frac{1}{N}\sum_{i=1}^{N}L_i(t)$ as show in Fig. **S9 b**. The $\boldsymbol{r^2(t)}$ and $\boldsymbol{L(t)}$ are fitted with linear functions. To eliminate the initial ballistic regime and box boundary effect, we did not include the first 50 ps and later 150 ps for linear fitting. All data can be fitted linearly, indicating that the diffusion follows a random walk mechanism.

According to random walk theory, the average step length a , which characterizes the mean distance traveled between changes in direction, can be calculated as $\boldsymbol{a}=\frac{\boldsymbol{r^2(t)}}{\boldsymbol{L(t)}}$ .Since both $\boldsymbol{r^2(t)}$ and $\boldsymbol{L(t)}$ should originate from zero, then $\boldsymbol{a}=\frac{\boldsymbol{k_L}}{\boldsymbol{k_{r^2}}}$, where k_L and k_{r^2} are the slop of the fitting line for $r^2(t)$ and $L(t)$, respectively. The effective path velocity v_{eff} , which characterizes the rate at which a particle accumulates trajectory length over time, is given by $v_{\text{eff}}=k_L=\frac{dL(t)}{dt}$. It also represents the average velocity per step. Therefore, the step time τ can be calculate as $\tau=\frac{a}{v_{eff}}$. Finally, the diffusivity of He is estimated using the Einstein equation: $D=\frac{k_{r^2}}{6}$. The calculated values of $v_{\text{eff}}, a, D\ and\ \tau$ are summarized in table S2.

Table S2. Diffusion parameters calculated from the 27 atoms simulation

	v_{eff}(Å/ps)	D (Å^2/ps)	a (Å)	τ (ps)
Ta	*6.80*	*1.40*	*1.24*	*0.182*
MoNbTa	*6.53*	*0.729*	*0.669*	*0.102*
MoNbTaVW	*4.97*	*0.101*	*0.122*	*0.0245*

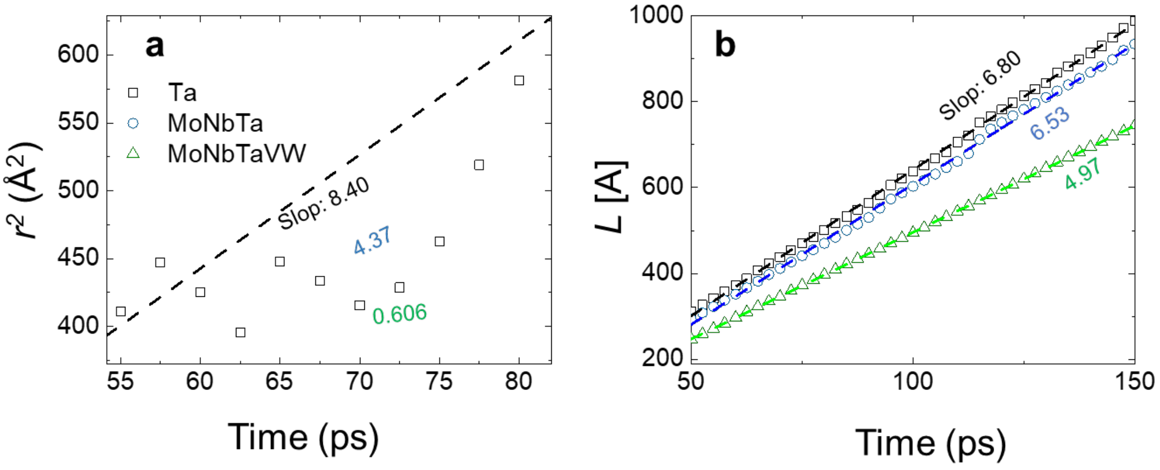

Fig.**S9** Average statistical results of the 27 He diffusion simulation : **a** mean squared displacement (r^2), **b** Trajectory length (L). The dash line in (a) and (b) shows the linear fitting.

5. Segregation effect

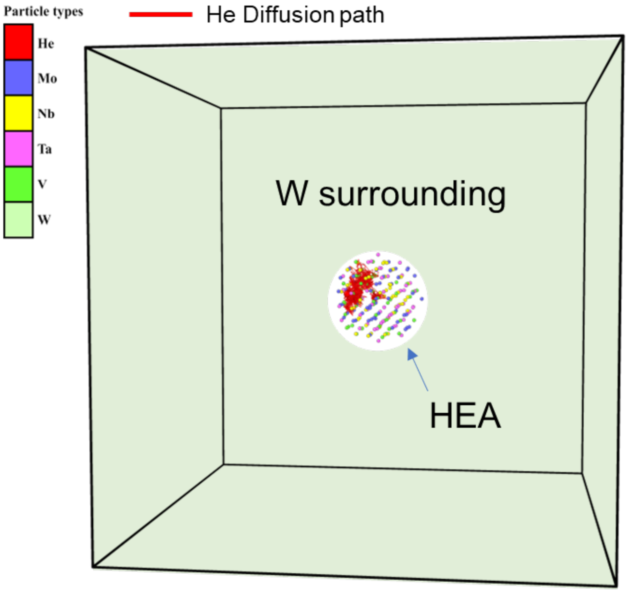

Fig.**S10**. Segregation effect in a W/HEA composite cell. Atomistic simulation box of bcc W (outer region) containing a central spherical HEA domain (Mo–Nb–Ta–V–W). A single He atom was inserted and then allowed to diffuse for 1000 ps at 1773 K. The red curve traces the He diffusion path.

To identify the affinity between He atoms and group-VI elements (W), we constructed a tungsten (W) simulation cell with a side length of 30 ***a***, where ***a*** = 3.185 Å denotes the lattice constant of W. The central spherical region of the cell (radius 10 Å) was replaced with a RHEA sphere, and a single He atom was placed at a tetrahedral interstitial site at the center of the sphere. The system was equilibrated, and the He atom was then allowed to diffuse for 1000 ps at 1773 K to monitor its migration pathway. The results are shown in Fig. **S10**. The He atom's trajectory was confined within the HEA sphere, providing additional evidence that He is attracted to the area rich in period-V elements (Mo, Nb, Ta) and avoids group-VI elements (W).

6. Videos

Supplementary Movie 1,2,3. Simulation of the diffusion of 27 He atoms in Ta, MoNbTa and MoNBTaVW over 500 ps.

Supplementary Movie 4,5,6. Simulation of the diffusion of single He atom in Ta, MoNbTa and MoNBTaVW over 700 ps.

Supplementary Reference

1. Senkov ON, Wilks GB, Miracle DB, Chuang CP, Liaw PK. Refractory high-entropy alloys. *Intermetallics* **18**, 1758-1765 (2010).

2. Gemmell DS. Channeling and related effects in the motion of charged particles through crystals. *Rev Mod Phys* **46**, 129-227 (1974).

3. Nordlund K, Djurabekova F, Hobler G. Large fraction of crystal directions leads to ion channeling. *Phys Rev B* **94**, (2016).

4. Schlueter K*, et al.* Absence of a Crystal Direction Regime in which Sputtering Corresponds to Amorphous Material. *Physical Review Letters* **125**, (2020).

5. Nordlund K. Molecular dynamics simulation of ion ranges in the 1–100 keV energy range. *Comput Mater Sci* **3**, 448-456 (1995).

6. Nordlund K, Lehtola S, Hobler G. Repulsive interatomic potentials calculated at three levels of theory. *Physical Review A* **111**, (2025).

7. Ziegler, James F., and Jochen P. Biersack. "The stopping and range of ions in matter." Treatise on heavy-ion science: volume 6: astrophysics, chemistry, and condensed matter. Boston, MA: Springer US, 1985. 93-129.

8. Nordlund K, Hobler G. Dependence of ion channeling on relative atomic number in compounds. *Nucl Instrum Methods Phys Res B* **435**, 61-69 (2018).